# A Dynamic Duo of Finite Elements and Material Points

Xuan Li UCLA USA xuan.shayne.li@gmail.com

Huamin Wang Style3D Research USA wanghmin@gmail.com Minchen Li Carnegie Mellon University USA minchernl@gmail.com

> Yin Yang University of Utah USA yin.yang@utah.edu

Xuchen Han Toyota Research Institute USA xuchen.han@tri.global

Chenfanfu Jiang UCLA USA chenfanfu.jiang@gmail.com





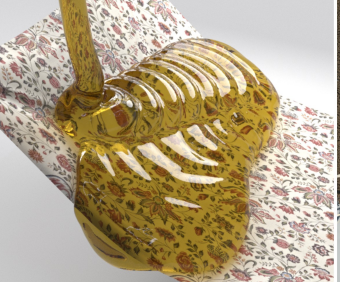




Figure 1: Multi-Material Simulations using Dynamic Duo. From left to right: a metal boat propelling through water; multicolored sand passing through holes in fabric; honey interacting with a textile surface; and a disaster caused by a debris flow. Each scene highlights the intricate interaction between different materials and structures, emphasizing the fidelity and adaptability of our coupled FEM-MPM simulator.

### **ABSTRACT**

This paper presents a novel method to couple Finite Element Methods (FEM), typically employed for modeling Lagrangian solids such as flesh, cloth, hair, and rigid bodies, with Material Point Methods (MPM), which are well-suited for simulating materials undergoing substantial deformation and topology change, including Newtonian/non-Newtonian fluid, granular materials, and fracturing materials. The challenge of coupling these diverse methods arises from their contrasting computational needs: implicit FEM integration is often favored to enjoy stability and large timesteps, while explicit MPM integration benefits from its allowance for efficient GPU optimization and flexibility of applying different plasticity models, which only allows for moderate timesteps. To bridge this gap, a mixed implicit-explicit time integration (IMEX) approach is proposed, utilizing principles from time splitting for partial differential equations and optimization-based time integrators. This method adopts incremental potential contact (IPC) to define a variational frictional contact model between the two materials, serving as the primary coupling mechanism. Our method enables implicit FEM

Permission to make digital or hard copies of all or part of this work for personal or classroom use is granted without fee provided that copies are not made or distributed for profit or commercial advantage and that copies bear this notice and the full citation on the first page. Copyrights for components of this work owned by others than the author(s) must be honored. Abstracting with credit is permitted. To copy otherwise, or republish, to post on servers or to redistribute to lists, requires prior specific permission and/or a fee. Request permissions from permissions@acm.org.

SIGGRAPH Conference Papers '24, July 27-August 1, 2024, Denver, CO, USA
© 2024 Copyright held by the owner/author(s). Publication rights licensed to ACM.
ACM ISBN 979-8-4007-0525-0/24/07...\$15.00
https://doi.org/10.1145/3641519.3657449

and explicit MPM to coexist with significantly different timestep sizes while preserving two-way coupling. Experimental results demonstrate the potential of our method as a strong foundation for future exploration and enhancement in the field of multi-material simulation.

### **CCS CONCEPTS**

• Computing methodologies → Physical simulation.

### **KEYWORDS**

optimization time integration, time splitting, finite element method, material point method, asynchronous time integration, frictional contact

#### **ACM Reference Format:**

Xuan Li, Minchen Li, Xuchen Han, Huamin Wang, Yin Yang, and Chenfanfu Jiang. 2024. A Dynamic Duo of Finite Elements and Material Points. In Special Interest Group on Computer Graphics and Interactive Techniques Conference Conference Papers '24 (SIGGRAPH Conference Papers '24), July 27-August 1, 2024, Denver, CO, USA. ACM, New York, NY, USA, 11 pages. https://doi.org/10.1145/3641519.3657449

### 1 INTRODUCTION

The Finite Element Method (FEM) has achieved notable success in animating elastic objects, such as solids, shells, and rods [Bergou et al. 2008; Grinspun et al. 2003; Teran et al. 2005]. Despite its advantages, FEM encounters challenges with severe deformations, often

resulting in an ill-conditioned system due to its total Lagrangian nature where the reference configuration is always at the initial time step. Furthermore, handling topology changes, particularly those induced by plasticity, remains a significant hurdle. To overcome these issues, researchers have proposed sophisticated re-meshing techniques [Bargteil et al. 2007; O'brien et al. 2002]. In contrast, the Material Point Method (MPM) employs a particle-based spatial discretization, simplifying the handling of topology changes. The auto-remeshing effect provided by the updated Lagrangian nature of MPM helps maintain a well-conditioned system even under severe deformations, where the reference configuration is at the previous time step. Additionally, MPM's 'plug-and-play' plasticity handling revolutionizes the animation of materials that undergo plastic deformations, such as snow, sand, foam, and fractures [Klár et al. 2016; Ram et al. 2015; Stomakhin et al. 2013; Wolper et al. 2019]. However, MPM requires a super-high resolution of particles to represent fine-detailed geometry, making it less efficient for simulating purely elastic objects than FEM, where adaptive meshing can be more effective.

This contrast between FEM and MPM underscores the need for their coupling in complex simulations, combining FEM's precision in geometry and elastic behavior with MPM's robustness in handling topological changes and plastic deformations. However, this coupling is not without challenges. FEM typically employs implicit time integration for stability, while explicit integration is favored in MPM, particularly for its ease in implementing plasticity models and because the computational cost of each matrix-vector multiplication in matrix-free implicit MPM is comparable to that of each explicit integration step. The time step sizes in these two integration methods can vary significantly, often by several orders of magnitude. Consequently, asynchronous coupling becomes essential to maintain their respective efficiencies. Another critical challenge is contact handling between the two domains. Contact force modeling is pivotal for two-way coupling, as it is the primary means of communication between the FEM and MPM domains.

To address these challenges, we propose a novel method to couple FEM and MPM. Our approach incorporates an asynchronous time splitting of FEM elasticity, MPM elastoplasticity, and interdomain frictional contact forces, leveraging the state-of-the-art Incremental Potential Contact (IPC) model [Li et al. 2020] to resolve contact forces between FEM surface triangles and MPM particles. Due to the high stiffness of the contact barrier in IPC, we couple FEM elasticity and inter-domain contact together by implicit integration under a large time step size. Observing the independent interaction of each particle with FEM bodies in this stage, we filter out non-colliding particles and apply a two-stage Newton's method, where elements are frozen once its solution accuracy is achieved, followed by the resolution of per-particle subproblems. After the implicit coupling, MPM elasticity is then explicitly integrated with a smaller time step size and can be combined with various plasticity models. In this stage, contact forces are treated as constant external forces, and friction integration is stabilized using Coulomb's friction law applied in each substep of MPM based on the current relative tangential velocity. We provide techniques to control penetrations due to time splitting and leverage a closest penetration-free state that is guaranteed to exist for visualization.

In summary, our technical contributions include:

- A novel framework for two-way coupling between meshed finite elements in arbitrary codimensions and meshless material points with arbitrary elastoplastic models.
- An asynchronous time-splitting scheme that effectively integrates implicit FEM and explicit MPM under significantly different time step sizes.
- Numerical treatments to accelerate particle-triangle contact resolutions within the implicit coupling step.
- An IPC-based MPM grid friction model that adheres to Coulomb's friction law.
- Techniques to reduce penetrations from splitting and guarantee penetration-free visualizations.

We demonstrate the effectiveness of our framework by simulating the coupling between FEM soft bodies, rigid bodies, and cloth with a wide range of MPM elastoplastic materials including water, sand, snow, and mud.

# 2 RELATED WORK

# 2.1 Finite Element Method

Pioneered by Terzopoulos et al. [1987], FEM has established itself as a fundamental technique for modeling elastic bodies in computer graphics. In recent physics-based animation research, robustness and efficiency have been critical. On the local level, robust constitutive models have been explored [Irving et al. 2004, 2006; Kim et al. 2019; Smith et al. 2018]. These models accommodate extreme deformations by allowing inverted or degenerated elements. On the global level, advancements have focused on developing new solvers for the governing nonlinear systems. Teran et al. [2005] introduced a method to project local Hessians to positive definite, thus greatly enhancing the stability of Newton's method. Gast et al. [2015] reformulated the nonlinear system into an optimization problem, enabling the use of line search for guaranteed convergence and allowing frame-rate time step sizes. Bouaziz et al. [2014]; Overby et al. [2017] solved the time integration through a local-global alternating minimization while maintaining a fixed global system Hessian. Trusty et al. [2022] employed a mixed variational finiteelement formulation and proposed an efficient solver. The domain decomposition technique has also been explored [Li et al. 2019; Wu et al. 2022]. On the other hand, FEM discretization has been successfully applied to co-dimensional objects, such as cloth [Baraff and Witkin 1998], shells [Chen et al. 2023; Grinspun et al. 2003], and rods [Bergou et al. 2008], and has been utilized to simulate rigid body dynamics through high-stiffness elasticity [Lan et al. 2022]. Flow-like and brittle materials can also be modeled [Bargteil et al. 2007; O'brien and Hodgins 1999; Wojtan and Turk 2008], though frequent remeshing is required to prevent locking artifacts and support topology changes. A fundamental problem in modeling FEM object interactions is contact handling. The state-of-the-art method, Incremental Potential Contact (IPC) [Li et al. 2020], uses a contact barrier to ensure interpenetration-free simulations. This method has been extended to simulate co-dimensional objects [Li et al. 2021]. IPC plays a vital role in our method to resolve FEM self-collisions and FEM-MPM inter-domain collisions.

#### 2.2 Material Point Method

MPM is a hybrid simulation method that combines Lagragian particles and Eulerian grids. Since its introduction to computer graphics [Hegemann et al. 2013; Stomakhin et al. 2013], it has revolutionized simulations involving large deformations and frequent topology changes. Researchers have focused on designing diverse plasticity models to simulate a variety of dynamic behaviors, including snow [Stomakhin et al. 2013], sand [Daviet and Bertails-Descoubes 2016; Klár et al. 2016], foam [Ram et al. 2015; Yue et al. 2015], viscoelastic rubber [Fang et al. 2019], phase changes [Stomakhin et al. 2014; Su et al. 2021], and damage [Fan et al. 2022; Wolper et al. 2020, 2019]. To overcome the limitations of Eulerian grids to represent detailed geometries, MPM can also be combined with meshes along with specially designed constitutive models [Fei et al. 2018, 2019, 2017; Han et al. 2019; Jiang et al. 2017]. In parallel, significant efforts have been made to enhance the efficiency of MPM. Fang et al. [2018] explored time-step adaptivity and optimized particle-grid transfers on sparse grids. Gao et al. [2017] introduced adaptive grids. Further optimizations of MPM on GPUs and distributed systems have been achieved by Fei et al. [2021]; Gao et al. [2018]; Qiu et al. [2023]; Wang et al. [2020b]. While implicit MPM offers guaranteed stability for frame-rate time integration, it requires sophisticated acceleration algorithms, such as multi-grid methods, to tackle the challenges posed by large-scale implicit nonlinear systems with large stencils [Wang et al. 2020a]. Additionally, the return mapping generally results in an asymmetric force Jacobian. This asymmetry necessitates intensive, model-by-model mathematical derivations to develop integrable equivalent force formulations [Li et al. 2022b] for robust implicit time integration.

### 2.3 FEM-MPM Coupling

The coupling between FEM and MPM has been extensively studied within the mechanical engineering community, driven by a shared motivation with this paper: to combine FEM's efficiency in modeling small deformations due to its use of adaptive meshing and MPM's suitability for simulating large deformations, including fractures. A common approach involved embedding FEM nodes into the MPM grid [Lian et al. 2011b]. However, this technique often leads to sticky contact at the FEM-MPM interface, a limitation inherited from MPM. To address this issue, Lian et al. [2011a] developed a separate grid contact model specifically for the interface. Another challenge arises from the requirement for consistent resolutions between the FEM discretization and the MPM grid. The particle-to-surface contact model emerged as an effective solution for this issue [Chen et al. 2015]. Despite these advancements, most of these coupling techniques rely on explicit time integration, requiring tiny step sizes for stability and thus overlooking the inherent efficiency of implicit FEM. This limitation has curtailed applications in computer graphics. Alternatively, Li et al. [2022a] explored particle-to-surface IPC to couple implicit FEM with implicit MPM in a monolithic manner. However, this method is confined to elastic objects, diminishing the necessity for coupling, and its computational efficiency is constrained by the implicit MPM bottleneck. Extending it to support general plasticity encounters similar challenges as those faced by implicit MPM. In contrast, our proposed mixed implicit-explicit time integration not only harnesses

the optimal efficiencies of both FEM and MPM but also maintains the flexibility to apply a diverse range of plasticity models.

# 3 GOVERNING EQUATIONS AND ASYNCHRONOUS TIME SPLITTING

The dynamics of a continuum  $\Omega$  can be characterized by a time-dependent deformation field  $\Phi(X,t)$  from the material space  $X \in \Omega$  to its current world space  $x \in \Omega^t$  at time t. This map is governed by conservation laws, including mass conservation and momentum conservation:

$$R(X,t)J(X,t) = R(X,0), \quad R(X,0)\frac{\partial V}{\partial t}(X,t) = f(X,t), \quad (1)$$

where R(X,t) is the mass density field,  $J(X,t)=\det \nabla_X \Phi(X,t)$  is the Jacobian determinant field,  $V(X,t)=\frac{\partial \Phi(X,t)}{\partial t}$  is the velocity field, and f(X,t) is the force density field. Here, we focus on two kinds of internal forces: elastic force, which is defined on the indomain deformation gradient  $F=\nabla_X \Phi(X,t)$  and frictional self-contact, which is defined on the domain boundary  $\partial \Omega$ , and omit external force for simplicity.

To illustrate the asynchronous time splitting techniques for multiple domains, we assume the continuum consists of two disjoint connected components:  $\Omega = \Omega_{\mathcal{A}} \cup \Omega_{\mathcal{B}}$ . Each domain has its own internal force field  $f_{\mathcal{A}}$  and  $f_{\mathcal{B}}$  (including elasticity and self-contact). We denote the inter-domain frictional contact force field as  $f_{\mathcal{A}\mathcal{B}}$ . We note that the time splitting is actually used to serialize the action of different forces on the whole domain  $\Omega$ , so we extend the definition of these forces to the entire domain with zero values.

From  $t^n$  to  $t^{n+1}$ , we would like to use different time integration schemes (and different spatial discretizations, which will be discussed later) for two elastic force fields: backward Euler for  $f_{\mathcal{A}}$  and forward Euler for  $f_{\mathcal{B}}$ . For stability consideration, the time integration of the frictional contact  $f_{\mathcal{A}\mathcal{B}}$  is bundled with  $f_{\mathcal{A}}$ . This leads to the following semi-discrete scheme for momentum conservation:

$$R^0(\hat{\boldsymbol{V}}^{n+1}-\boldsymbol{V}^n)=h(\hat{f}_{\mathcal{A}}^{n+1}+\hat{f}_{\mathcal{AB}}^{n+1}) \qquad \qquad \text{(backward Euler), (2a)}$$

$$R^{0}(\mathbf{V}^{n+1} - \hat{\mathbf{V}}^{n+1}) = h \mathbf{f}_{\mathcal{Q}}^{n}$$
 (forward Euler), (2b)

where the superscript stands for the discrete time step,  $R^0 = R(X,0)$ ,  $h = t^{n+1} - t^n$  is the time step size and  $\hat{V}^{n+1}$  is an intermediate state. Note that Equation (2b) has no impact on  $\Omega_{\mathcal{A}}$ , so we have  $V_{\mathcal{A}}^{n+1} = \hat{V}_{\mathcal{A}}^{n+1}$ , meaning that there is no extra time integration process on  $\Omega_{\mathcal{A}}$ . And the equation is simplified to:

$$R_{\mathcal{B}}^{0}(V_{\mathcal{B}}^{n+1} - \hat{V}_{\mathcal{B}}^{n+1}) = hf_{\mathcal{B}}^{n}. \tag{3}$$

On the other hand, there is only contact force  $f_{\mathcal{AB}}$  acting on  $\Omega_{\mathcal{B}}$  in Equation (2a), which leads to

$$R_{\mathcal{B}}^{0}\hat{V}_{\mathcal{B}}^{n+1} = h\hat{f}_{\mathcal{A}\mathcal{B}}^{n+1} + R_{\mathcal{B}}^{0}V_{\mathcal{B}}^{n}. \tag{4}$$

Then Equation (2b) can be rewritten as

$$R_{\mathcal{B}}^{0}(V_{\mathcal{B}}^{n+1} - V_{\mathcal{B}}^{n}) = h(\hat{f}_{\mathcal{A}\mathcal{B}}^{n+1} + f_{\mathcal{B}}^{n}). \tag{5}$$

Intuitively, the above equation can be understood that  $\hat{f}_{\mathcal{AB}}^{n+1}$  from Equation (2a) is treated as a constant external force in Equation (2b).

However, forward Euler usually requires much smaller time step sizes compared with backward Euler for stability considerations. This motivates us to use asynchronous time splitting. Assume  $\tilde{h}=h/N$  is the time step size required by stability. The one-step forward

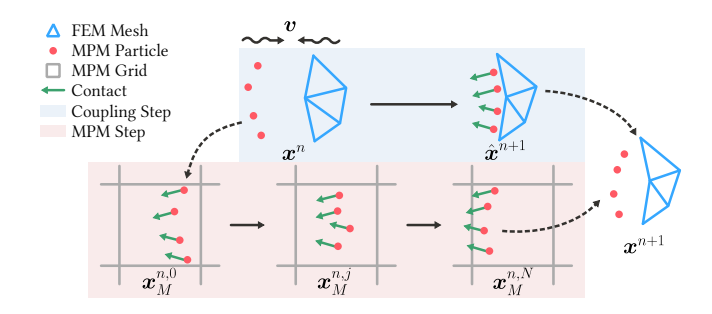


Figure 2: Illustration of the Dynamic Duo. We couple FEM-MPM inter-domain contact with FEM elasticity by implicit integration. This contact force is then applied as a constant external Lagrangian force on MPM particles throughout N substeps of explicit MPM integration.

Euler time integration eq. (5) on  $\Omega_{\mathcal{B}}$  can be further decomposed into N substeps, leading to the following asynchronous time-splitting scheme:

$$R^{0}(\hat{V}^{n+1} - V^{n}) = h(\hat{f}_{\mathcal{A}}^{n+1} + \hat{f}_{\mathcal{A}\mathcal{B}}^{n+1}), \tag{6a}$$

$$V_{\mathcal{A}}^{n+1} = \hat{V}_{\mathcal{A}}^{n+1},\tag{6b}$$

$$R^{0}(V_{\mathcal{B}}^{n,j+1}-V_{\mathcal{B}}^{n,j})=\frac{h}{N}(\hat{f}_{\mathcal{A}\mathcal{B}}^{n+1}+f_{\mathcal{B}}^{n,j}), \quad j=0,1,2,...,N-1, \ \ (6c)$$

$$V_{\mathcal{B}}^{n+1} = V_{\mathcal{B}}^{n,N}, \quad V_{\mathcal{B}}^{n,0} = V_{\mathcal{B}}^{n}.$$
 (6d)

### 4 DYNAMIC DUO

In this section, we illustrate how two different spatial discretizations, the Finite Element Method (FEM) and the Material Point Method (MPM), work together seamlessly. We show the time-stepping pipeline in Algorithm 1 and in Figure 2. Following the convention above, we discretize  $\Omega_{\mathcal{A}}$  with FEM meshes and  $\Omega_{\mathcal{B}}$  with MPM particles. The inter-domain frictional contact forces are defined between the FEM mesh surface and MPM particles using the Incremental Potential Contact (IPC) method [Li et al. 2020]. The significant advantage of explicit MPM, and the primary motivation behind this work, is that explicit MPM can be highly optimized for efficiency and can incorporate different plasticity models without the need for tediously deriving integrable plastic forces [Li et al. 2022b].

# 4.1 Notations

Let  $x_{\star}, v_{\star}$  with  $\star \in \{F, M\}$  be the nodal positions and velocities of FEM/MPM bodies. Here,  $\{x_F, v_F\}$  are defined on FEM mesh vertices, and  $\{x_M, v_M\}$  are defined on MPM particles.  $x = [x_F, x_M], v = [v_F, v_M]$  are their concatenations. A superscript n can be appended to distinguish different time steps. Viewing the initial positions  $X = x^0$  as the material space,  $x^n$  is the approximation of  $\Phi(X, t^n)$ , and  $v^n$  is the approximation of  $\frac{\partial}{\partial t}\Phi(X, t^n)$ . Let  $M = \mathrm{Diag}(M_F, M_M)$  be the global diagonal lumped mass matrix formed by integrating R(X, t) over individual FEM elements or MPM particles,  $\{\hat{x}, \hat{v}\}$  be the intermediate penetration-free state from the coupling step guaranteed by IPC, and  $h_M, h = Nh_M$  be the time step sizes for MPM and FEM, respectively. We distinguish  $\hat{x}$  and x because, after the MPM integration,  $x_M$  may penetrate into  $x_F$ , as discussed in Section 4.4. In addition,  $\hat{x}$  serves as a feasible initial guess for the

coupling step and the state at which to evaluate friction basis in the IPC model.

# 4.2 Implicit Coupling Step

In this step, we conceptualize MPM particles as discrete rigid spheres with radius r excluding self-contact. The contact acts in a thin layer enveloping the sphere [Li et al. 2021]. We take  $r = \Delta x/\sqrt[3]{\text{PPC}}$  where  $\Delta x$  is the spacing of the MPM background grid, and PPC stands for particle number per cell. This allows overlaps between particles to prevent unrealistic penetrations of sharp FEM parts into MPM bodies. After spatial discretization, the elastic and contact forces in the momentum equation (Equation (6a)) are defined w.r.t. the positions of vertices and particles, necessitating a time discretization of  $\frac{\partial}{\partial t}\Phi(X,t)=V(X,t)$ . Employing the backward-Euler method, the spatially integrated governing equations are discretized as follows:

$$\begin{split} \boldsymbol{M}(\hat{\boldsymbol{v}}^{n+1} - \boldsymbol{v}^n) &= h(f^E(\hat{\boldsymbol{x}}_F^{n+1}) + f^{SC}(\hat{\boldsymbol{x}}_F^{n+1}) + f^C(\hat{\boldsymbol{x}}^{n+1}) + M\boldsymbol{g}), \\ \hat{\boldsymbol{x}}^{n+1} &= \boldsymbol{x}^n + h\hat{\boldsymbol{v}}^{n+1}. \end{split} \tag{7}$$

Here, the elasticity force  $f^E$  is represented by the negative gradient of elastic strain energies. This includes various forms of energy: volumetric elasticity energy on tetrahedra for modeling soft bodies; membrane and bending energies on triangles for thin shells; and rigidity energy defined per body to model nearly rigid objects [Lan et al. 2022]. The self-contact  $f^{SC}$  and the inter-domain contact  $f^C$ , defined among MPM particles and FEM surfaces, are derived from the negative gradients of frictional contact potentials [Li et al. 2020].

Following [Li et al. 2020], the governing nonlinear equation system can be integrated into an optimization problem w.r.t. nodal positions:

$$\hat{\mathbf{x}}^{n+1} = \operatorname{argmin}_{\mathbf{x}} \frac{1}{2} \|\mathbf{x} - \tilde{\mathbf{x}}^{n+1}\|_{\mathbf{M}}^{2} + h^{2}(\Psi(\mathbf{x}_{F}) + B(\mathbf{x}) - \mathbf{x}^{\top} \mathbf{M} \mathbf{g}).$$
(8)

Here,  $\tilde{x}^{n+1} = x^n + v^n h$  represents the predictive position under inertia,  $\Psi$  denotes the elastic potential of FEM bodies, and B is the frictional contact potential. Notably, after the MPM step in the previous time step, there might be slight penetrations in  $x^n$ . So we use  $\hat{x}^n$  instead of  $x^n$  as the starting configuration for the optimization. After solving this optimization, the positions and velocities of FEM vertices are updated accordingly to  $x_F^{n+1} = \hat{x}_F^{n+1}, v_F^{n+1} = \hat{v}_F^{n+1}$ . It is important to note that MPM particles are not advected in this step to avoid inconsistencies between tracked deformation gradients and particle positions. This optimization problem is solved using Newton's method with a backtracking line search, where the initial step size is determined by continuous collision detection (CCD) to prevent penetration during the optimization process [Li et al. 2020]. When assembling the global Hessian matrix, local Hessians are projected to be semi-positive definite to guarantee an energydecreasing direction. The linear system is solved by the Conjugate Gradient (CG) method preconditioned by the  $3 \times 3$  diagonal blocks.

Non-colliding Particle Filtering. Due to the inherent nature of MPM, the number of MPM particles significantly exceeds the number of FEM vertices. However, a large proportion of particles do not even collide with FEM bodies during a time step. For these non-colliding particles, their next state of non-penetration,  $\hat{x}^{n+1}$ , can be analytically determined as  $\tilde{x}^{n+1}$ , and they do not interfere

## Algorithm 1 Dynamic Duo Time Stepping

Scale MPM particle masses by  $\frac{2N}{N+1}$ ; // Section 4.4 Implicit coupling; // Section 4.2 Update FEM states; Restore MPM particle masses; // Explicit MPM step (Section 4.3): Evaluate particle contact forces ( $f^{CN}$ ,  $f^{CT}$ ) and basis velocity  $v^B$ ;

for j = 1, 2, ..., N do

Particle-to-grid transfer of mass, velocity, elasticity, contact, friction, and basis velocity;

Update grid velocity by explicit integration of elasticity and contact;

Apply Coulumb's friction law to grid velocity; Grid-to-particle transfer to update MPM states;

end for

with other particles or FEM bodies. To optimize computational resources, we can safely exclude these non-interacting degrees of freedom in Equation (8). To do the filtering, we only keep particles that have potential collisions as the scene moves from  $x^n$  to  $x^n + 2h(v^n + gh)$ . The collisions are detected by checking overlaps between trajectories' bounding boxes.

Two-stage Newton's Method. To further accelerate convergence, we employ a two-stage Newton's method. In the first stage, we solve the full nonlinear optimization until the residual on FEM DOFs reaches the desired tolerance. We then freeze FEM bodies and continue to optimize the particle DOFs. A key observation is that once the FEM domain is fixed, the entire optimization problem can be effectively divided into independent sub-problems for each particle. However, direct per-particle optimization is not trivial to implement on a GPU since the contact pairs may vary over time. Instead, we still simultaneously search for all particles, but with several acceleration techniques:

- The system matrix is now 3 × 3 block-diagonal, consisting only of the diagonal mass matrix and the diagonal blocks of the barrier Hessian. The inverse of the Hessian can then be efficiently evaluated per diagonal block.
- For the backtracking line search, we perform CCD to clamp the search directions per particle and then only halve perparticle step sizes on energy-increasing particles.
- We continue to freeze particles that reach the desired accuracy because of the independence of particles.

### 4.3 Explicit MPM Step

Due to the asynchronous time splitting, each time step comprises N sub-steps of explicit MPM integration. At the end of the coupling step, the IPC force  $f^C$  is evaluated on particles, which is decomposed as the sum of a normal contact force  $f^{CN}$  and a tangential friction force  $f^{CT}$ .  $f^{CN}$  is then treated as a constant Lagrangian external force applied to the particles.  $f^{CT}$ , requiring special consideration, will be discussed in a separate section. We follow MLS-MPM [Hu et al. 2018] for our explicit MPM sub-stepping. Each particle's state

is described by a four-tuple  $(x_p, v_p, C_p, F_p^E)$ :  $x_p$  denotes the particle position,  $v_p$  the particle velocity,  $F_p^E$  the elastic deformation gradient tracked on the particle, and  $C_p$  the angular momentum matrix [Jiang et al. 2015]. Time integration within MPM occurs on a background grid. At each substep j, from  $t^n$  to  $t^{n+1}$ , particle mass and velocity are transferred to the grid:

$$m_{i}^{j} = \sum_{p} m_{p} w_{ip}^{j}, \quad v_{i}^{j} = \frac{1}{m_{i}^{j}} \sum_{p} w_{ip}^{j} m_{p} (v_{p}^{j} + C_{p}^{j} (x_{i} - x_{p}^{j})), \quad (9)$$

where  $x_i$  is the position of grid node i,  $w_{ip}^j$  represents a quadratic MLS basis defined at grid node i evaluated at  $x_p^j$ ,  $m_i^j$  is the transferred grid node mass, and  $v_i^j$  is the transferred grid velocity. For simplicity, we have omitted the superscript n in Equation (6c). The discretized momentum equation on the grid, Equation (6c), is expressed as  $v_i^{j+1} = v_i^j + h_M f_i^j/m_i^j$ , where the grid  $f_i^j$  is the sum of the transferred normal contact force  $f_i^{CN,j} = \sum_p w_{ip}^j f_p^{CN}$ , gravity force  $m_i^j g$  and elasticity force  $f_i^{E,j} = \sum_p V_p^0 \tau(F_p^{E,j}) \nabla w_{ip}^j$ , where  $\tau$  is the Kirchhoff stress. In MLS-MPM, the gradient of the weight function is calculated as  $\nabla w_{ip}^j = \frac{4}{\Delta x^2} w_{ip}^j (x_i - x_p^j)$ . The updated grid velocities are then transferred back to the particles, updating their states:

$$v_{p}^{j+1} = \sum_{i} v_{i}^{j+1} w_{ip}^{j}, \quad x_{p}^{j+1} = x_{p}^{j} + h_{M} v_{p}^{j+1},$$

$$C_{p}^{j+1} = \sum_{i} v_{i}^{j+1} \nabla w_{ip}^{j,\top}, \quad F_{p}^{E,j+1} = (I + h_{M} C_{p}^{j+1}) F_{p}^{E,j}.$$
(10)

Incorporating plasticity, at the end of each MPM substep, we further pull  $F_p^{E,j+1}$  back into a predefined elastic region using the associated return mapping  $F_p^{E,j+1} \leftarrow \mathcal{Z}(F_p^{E,j+1})$  [Jiang et al. 2016].

MPM Friction. In accordance with physical principles, the friction force should always oppose the relative tangential velocity without altering its direction. Naively applying the evaluated tangential friction force  $f^{CT}$  on particles can easily violate this law, causing high-frequency vibration of MPM objects that should remain stationary. To stabilize friction integration, we transfer the basis velocity (defined as the nearby FEM surface velocity) onto the grid. This basis velocity is estimated at the coupling solve's convergence by interpolating the velocities of the friction basis onto MPM particles and then transferred onto grid to serve as the basis velocity for grid nodes:

$$v_p^B = \frac{\sum_{k \in T} \lambda_{k,p} v_k}{\sum_{k \in T} \lambda_{k,p}}, \quad v_i^{B,j} = \frac{\sum_p w_{ip}^j v_p^B}{\sum_{p, f_p^{CT} \neq 0} w_{ip}^j}.$$
 (11)

Here T is the set of contact pairs contributing to friction,  $\lambda_{k,p}$  denotes the magnitude of the normal contact force, and  $v_k$  is the velocity at the closest point to particle p on the contacting triangle. The need for interpolation arises from the presence of multiple contact pairs that collectively contribute to the total friction force  $f^{CT}$  on particle p. Note that this averaging process only includes particles experiencing nonzero friction force, and we skip node i if the denominator is zero. We define the tangential relative velocity on the grid as:

$$\boldsymbol{v}_{i}^{\mathrm{rel},j+1} = (\boldsymbol{I} - \boldsymbol{n}\boldsymbol{n}^{\top})(\boldsymbol{v}_{i}^{j+1} - \boldsymbol{v}_{i}^{B,j}), \tag{12}$$

where n is the normalized  $f_i^{CN,j}$  and  $v_i^{j+1}$  is the velocity after applying elasticity and normal contact. The final grid velocity, as adjusted by Coulomb's friction model, is given by:

$$v_i^{j+1} \leftarrow v_i^{j+1} - \min\{\|\Delta v_i^{CT,j}\|, \|v_i^{\text{rel},j+1}\|\} v_i^{\text{rel},j+1}/\|v_i^{\text{rel},j+1}\|, \quad (13)$$

where  $\Delta v_i^{CT,j} = f_i^{CT,j} h_M/m_i$  is the velocity increment resulting from  $f_i^{CN}$  if treated as an external force. Note that the friction coefficients are already utilized to evaluate  $f^{CT}$ , which may be assembled from interfaces with different friction coefficients. The projection can be understood that the application of  $f_i^{CT,j}$ , clamped by  $\|v_i^{\mathrm{rel},j+1}\|$ . This approach effectively ensures that the friction force opposes the relative velocity direction and does not change it. Our handling of friction represents a balance between conserving momentum and maintaining stability, with the latter being more crucial for visual effects. Note that the above friction-related quantities on particles are evaluated at  $\hat{x}$ .

## 4.4 Reducing Penetrations from Splitting

Using a first-order scheme, such as symplectic Euler and backward Euler, the integration of  $\frac{D}{Dt}V(X,t)=a$  with a constant acceleration a will yield the same velocity despite varying time step sizes. However, this consistency does not extend to the integration of  $\frac{D}{Dt}\Phi(X,t)=V(X,t)$ . It is a common observation that, under constant gravity acceleration and using a first-order scheme, objects fall faster with larger time step sizes. This mismatch contributes to the penetrations of MPM particles into FEM bodies. Higher-order schemes may be employed to reduce this mismatch, but they complicate the implementation. Instead, we stick to backward Euler and symplectic Euler coupling for implementation simplicity but propose methods to reduce penetrations due to splitting.

Let the evaluated contact acceleration on a particle be a at coupling step convergence. Ignoring elasticity, from  $t^n$  to  $t^{n+1}$ , the trial velocity and the final velocity are the same:  $\hat{v}^{n+1} = v^{n+1} = v^n + ha$ . However, this does not apply to positions. After implicit time integration, the penetration-free position is  $\hat{x} = x^n + hv^n + h^2a$ . In contrast, using symplectic Euler (ignoring elasticity) with a time step of  $\frac{h}{N}$ , the final position is  $x^{n+1} = x^n + \frac{h}{N} \sum_{j=1}^N (v^n + \frac{jh}{N}a) = x^n + hv^n + \frac{N+1}{2N}h^2a$ .

One effective way to reduce the mismatch is to decrease h, as the error is  $O(h^2)$ . The error order might be slightly lower in practice due to the splitting of MPM elasticity and smoothing from particle-grid transfers. Additionally, we employ a plug-and-play mass scaling mechanism and visualize the closest non-penetration states to eliminate penetration artifacts.

Mass Scaling. The principle behind this mechanism is to slightly increase the contact force, repelling MPM solids further away from FEM solids. To reduce penetrations in  $\mathbf{x}^{n+1}$ , we can scale the contact force f by  $\frac{2N}{N+1}$  in the MPM step, to align new  $\mathbf{x}^{n+1}$  with beforescaling  $\hat{\mathbf{x}}$ . However, scaling f during the implicit coupling is also necessary to ensure FEM receives an equivalent momentum correction. This is challenging since f is an implicit force in the coupling step. A solution comes from our discovery that a particle's contact force at equilibrium is approximately proportional to its mass. We scale the particle masses by  $\frac{2N}{N+1}$  when solving the implicit coupling, and then restore the original masses during MPM integration. Note

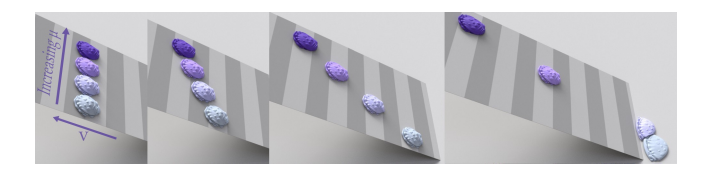


Figure 3: MPM Friction. MPM Play-Dohs with different friction coefficients on an incline conveyor.

that the contact force is still an internal force, not interfering with the total momentum. With this scaling, there will be a greater gap between two domains in  $\hat{x}$ , leading to fewer penetrations in  $x^{n+1}$ .

Non-penetration External State. To visually address penetrations, we use a separate external state of particles  $\boldsymbol{x}_M^{o,n+1}$  solely for rendering purposes.  $\hat{\boldsymbol{x}}_M^{n+1}$  lags one time step behind the current state, while the current state  $\boldsymbol{x}_M^{n+1}$  may have penetrations. So we visualize  $\boldsymbol{x}_M^{o,n+1}$  by freezing FEM solids and performing a per-particle CCD from  $\hat{\boldsymbol{x}}_M^{n+1}$  to  $\boldsymbol{x}_M^{n+1}$  to find a closest non-penetration state. We only compute an external state per frame for visualization because this state is not used in time stepping.

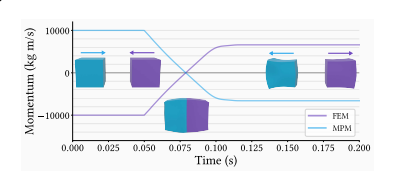
### 5 EVALUATION

We implemented our framework on a workstation with an NVIDIA RTX 6000 Ada GPU and an Intel Core i9-10920X CPU. The relative error of CG is set to  $10^{-3}$ . We stop Newton's method if the  $L_{\infty}$  norm of the search direction reaches below  $10^{-2}h$  m.

# 5.1 Ablation Studies and Unit Tests

Momentum Conservation.

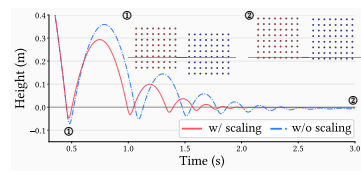
The system's linear momentum is conserved in the absence of friction and external forces. To demonstrate this, we conduct an experiment involving two cubes with identical prop-



erties but different discretizations. These cubes collide under the same velocity magnitudes. As shown on the right, the total linear momentum remains consistently zero. However, we note that the linear momentum under friction will not be conserved due to our friction clamping mechanism, and the angular momentum is not conserved due to the choice of backward Euler.

Reducing Penetrations. Our

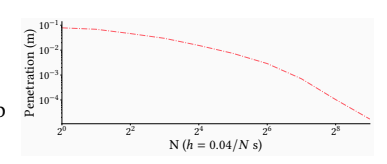
mass scaling mechanism can effectively reduce the penetration of the MPM internal state into FEM bodies. In a 2D experiment, an elastic cube is allowed to free fall from a height of



1 meter onto the ground with a relatively large time step size,  $h = 10^{-2}$ s. As depicted in the inset figure, we compare scenarios with and without mass scaling. The results reveal the mechanism's

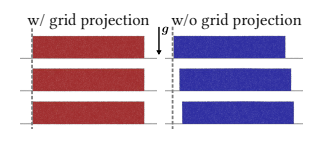
efficacy in reducing penetration. Additionally, a notable side effect of mass scaling is its contribution to stabilizing objects on the ground.

Furthermore, reducing the time step size is another effective way to mitigate penetrations. Under the same experimental setup above, we progressively refined the time step size by a factor of 2. The inset plot



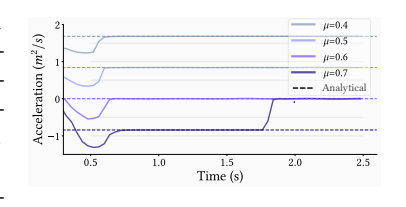
demonstrates that penetration can effectively converge to zero with this continuous refinement of the time step size.

MPM Friction. We conduct a 2D experiment to validate our friction projection on the MPM grid. A rectangular elastic object is placed on a horizontal plane under downward gravity. Despite utilizing a small time step size



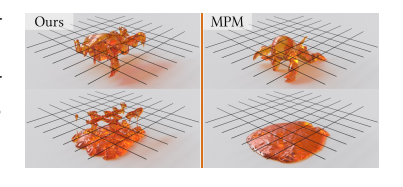
 $(h = 10^{-3} \text{s})$ , the object vibrates on the plane if we directly apply friction as a constant external force, as shown on the right in the inset figure. However, by applying our projection on the MPM grid, we effectively address this issue, shown on the left of the inset figure.

To further assess the accuracy of our friction model, we conduct an experiment where a conveyor with an inclined angle  $\theta = \arctan(0.6)$  tries to move 4 MPM Play-Dohs upward, as shown in Figure 3. Each body, with von



Mises plasticity, is assigned a distinct friction coefficient ( $\mu$  = 0.4, 0.5, 0.6, 0.7). The experiment confirms that our model can resolve both static and dynamic friction even on moving interfaces. The inset plot reveals that the accelerations from the dynamic friction align with the analytical solution  $g(\sin \theta^* - \mu \cos \theta^*)$  (downward positive direction,  $\theta^*$  = arctan  $\mu$ ). We successfully capture the transition from dynamic to static friction when  $\mu$  = 0.7 as the relative velocity vanishes.

FEM Boundary in MPM. In traditional MPM, boundary conditions are typically enforced via fuzzy, grid-based collision detection, which may overlook fine geometrical details close to the grid resolution. In con-



trast, CCD in our method can resolve collisions with objects of any thickness, independent of the MPM grid resolution. Illustrated in the inset figure, we compare our approach with traditional MPM in a scenario where a mass of viscous fluid falls onto a thin wire mesh. With our method, the fluid successfully adheres to the wires due to



Figure 4: Boat. An FEM boat's progression through MPM water.

friction, whereas traditional MPM fails to capture the interaction between the fluid and the wire mesh.

### 5.2 Multi-Material Simulation

In this section, we conduct a comprehensive evaluation of the Dynamic Duo on its performance in twoway coupled simulations involving a diverse set of FEM elastic solids, such as soft bodies, rigid bodies,

	h (s)	$h_M$ (s)	s/step	#P (×10 <sup>6</sup> )	#V (×10 <sup>3</sup> )
Boat	2e-3	5e-5	3.81	3.12	10.2
Ruts	2e-3	2e-5	3.70	2.80	38.0
Dough	2e-5	2e-5	0.67	0.727	10.7
Snowball	5e-3	5e-5	2.22	2.14	2.66
Honey	2e-3	1e-5	1.72	1.19	29.2
Colored Sand	2e-3	2e-5	11.7	5.57	38.4
Debris Flow	5e-3	5e-5	6.71	1.47	236

cloth, and various MPM elastoplastic materials, including fluid, sand, snow, and debris flow. Detailed simulation statistics can be found in the inset table. The average timing per step is reported. The last two columns are the particle count and the vertex count.

Boat. In Figure 4, we demonstrate the use of affine body dynamics [Lan et al. 2022] to simulate the movement of a rigid boat through a tank filled with J-based MPM fluid [Jiang et al. 2015]. The propeller is attached to the shaft through contact. Buoyancy keeps the boat afloat. The interaction between the propeller and the water generates forward thrust by pushing the water backward. The propeller is not controlled by Dirichlet boundary conditions. Instead, the effect of motor power on the propeller is mimicked by a balanced rotational external force field to generate a naturalistic interaction between the propeller and the boat.

Ruts. In Figure 8, we present an experiment, inspired by Zhao et al. [2023a], to demonstrate our Dynamic Duo's potential applications in geotechnical engineering, particularly in analyzing soil interactions. We simulate a scenario of a NASA Mars rover's wheel

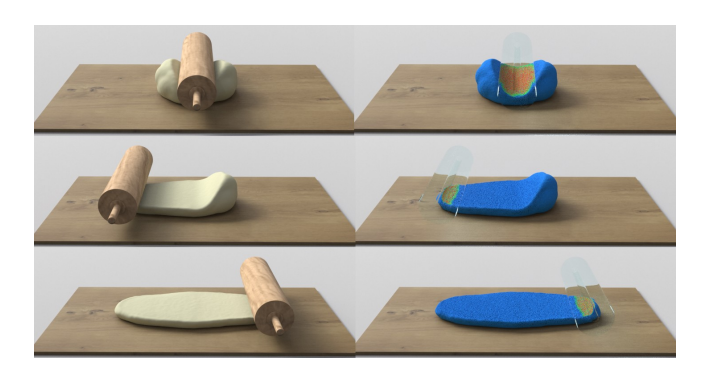
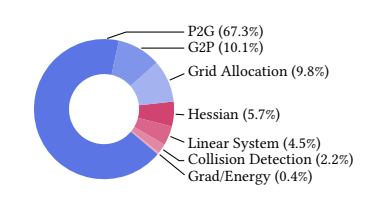


Figure 5: Dough. A rolling pin rolls out an MPM dough. Contact force is visualized on particles by a color gradient ranging from blue (low) to red (high).

traversing granular soil modeled using MPM with Drucker-Prager plasticity, thus leaving deep ruts. Similar to the previous example, the wheel's movement is driven by a balanced rotational external force field. Notably, we haven't introduced additional friction between the soil and the wheel; instead, the thrust is generated solely through the friction amongst the soil grains themselves.

Dough. In Figure 5, we simulate a common kitchen task to demonstrate the application of rigid bodies in soft body manipulation, inspired by [Huang et al. 2021]. A rolling pin flattens MPM dough with von Mises plasticity. The rolling pin's handle follows a predefined path, while the roller is attached around it by contact, free to rotate. The two-way interaction is indicated by the rotation driven by friction between the dough and the roller.

Snowball. In Figure 7, we drop an MPM snow ball modeled with Cam-Clay plasticity [Gaume et al. 2018] onto soft FEM mushrooms. The two-way impact smashes the snowball and also deforms the elastic mushrooms. Addition-



ally, due to friction, portions of the snow adhere to the tops of the mushrooms. Notably, as detailed in the inset pie chart, the computational cost of contact handling (red) in this scenario is relatively moderate compared to MPM time integration (blue).

Honey. In Figure 6, we present a simulation where honey is poured over pieces of cloth, each having different friction coefficients. The dynamics of the cloth are captured using ARAP membrane energy and dihedral bending energy [Grinspun et al. 2003], and the honey is modeled as MPM J-based fluids with viscosity. The varying magnitudes of friction result in distinct buckling patterns on the cloth.

Colored Sand. In Figure 9, we showcase a simulation where a pile of colored sand, modeled using Drucker-Prager plasticity, is scooped up by a cloth. The sand grains slowly trickle out through small, pre-opened holes. Subsequently, the sand is released, burying

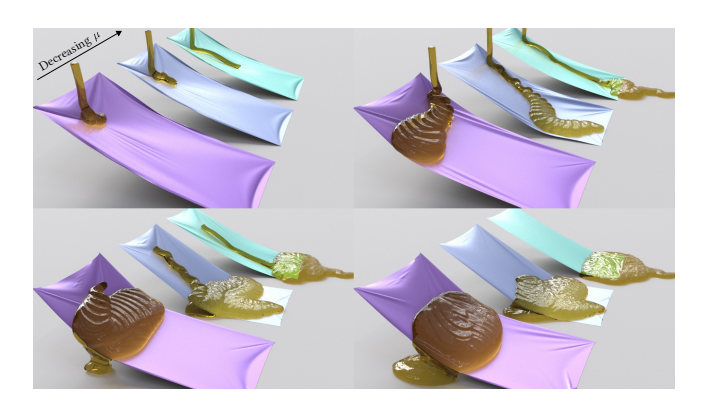


Figure 6: Honey. Different buckling patterns of honey on a piece of cloth with different friction coefficients.

a corner of the cloth. The rich collisions between the cloth and sand grains demonstrate the robustness of our coupling framework.

Debris Flow. In our final example, depicted in Figure 10, we simulate a large-scale natural disaster involving a debris flow. The flow, modeled using von Mises plasticity with softening [Zhao et al. 2023b], cascades down a terrain of complex geometry. The tremendous kinetic energy of the debris flow not only causes significant deformation of trees but also washes rocks down the valley.

#### 6 CONCLUSION

We introduced the Dynamic Duo, a novel framework designed to integrate finite elements and material points seamlessly. The IMEX framework combines the optimal performance of implicit FEM and the flexibility of explicit MPM in applying various plasticity models. We achieve this through an asynchronous time-splitting scheme, where IPC is applied to model inter-domain frictional contact between FEM and MPM. The Dynamic Duo is not only pivotal for creating complex multi-material animations but also holds potential in inverse applications such as shape optimization, robot learning, and disaster prediction and prevention. However, our framework also presents certain limitations that warrant further research. For instance, friction clamping can underestimate the friction forces on MPM bodies. Tracking momentum loss and applying correction impulses to FEM could be explored. Moreover, completely eliminating the penetration issue in an efficient way is yet to be achieved. Future developments could explore alternating FEM and MPM integrations to incrementally resolve residual penetrations. Additionally, optimizing the coupling step is another avenue for improvement, possibly through more efficient Hessian assemblies and linear solvers.

### **ACKNOWLEDGMENTS**

We sincerely thank the anonymous reviewers for their valuable feedback. We thank Pingying Chen for narrating the video. We acknowledge support from NSF (2301040, 2008915, 2244651, 2008564, 2153851, 2023780), UC-MRPI, Sony, Amazon, and TRI.

#### REFERENCES

- David Baraff and Andrew Witkin. 1998. Large steps in cloth simulation. In Proceedings of the 25th annual conference on Computer graphics and interactive techniques. 43–54.
- A. W. Bargteil, C. Wojtan, J. K. Hodgins, and G. Turk. 2007. A finite element method for animating large viscoplastic flow. *ACM Trans. Graph.* 26, 3 (2007), 16–es.
- Miklós Bergou, Max Wardetzky, Stephen Robinson, Basile Audoly, and Eitan Grinspun. 2008. Discrete elastic rods. In ACM SIGGRAPH 2008 papers. 1–12.
- S. Bouaziz, S. Martin, T. Liu, L. Kavan, and M. Pauly. 2014. Projective dynamics: Fusing constraint projections for fast simulation. ACM Trans. Graph. 33, 4 (2014), 1–11.
- Y. Chen, T. Xie, C. Yuksel, D. Kaufman, Y. Yang, C. Jiang, and M. Li. 2023. Multi-Layer Thick Shells. In ACM SIGGRAPH Conference Proceedings. 1–9.
- ZP Chen, XM Qiu, X Zhang, and YP Lian. 2015. Improved coupling of finite element method with material point method based on a particle-to-surface contact algorithm. Computer Methods in Applied Mechanics and Engineering 293 (2015), 1–19.
- G. Daviet and F. Bertails-Descoubes. 2016. A semi-implicit material point method for the continuum simulation of granular materials. ACM Trans. Graph. 35, 4 (2016).
- Linxu Fan, Floyd M Chitalu, and Taku Komura. 2022. Simulating brittle fracture with material points. ACM Transactions on Graphics (TOG) 41, 5 (2022), 1–20.
- Yu Fang, Yuanming Hu, Shi-Min Hu, and Chenfanfu Jiang. 2018. A temporally adaptive material point method with regional time stepping. In *Computer graphics forum*, Vol. 37. Wiley Online Library, 195–204.
- Yu Fang, Minchen Li, Ming Gao, and Chenfanfu Jiang. 2019. Silly rubber: an implicit material point method for simulating non-equilibrated viscoelastic and elastoplastic solids. ACM Transactions on Graphics (TOG) 38, 4 (2019), 1–13.
- Y. Fei, C. Batty, E. Grinspun, and C. Zheng. 2018. A multi-scale model for simulating liquid-fabric interactions. ACM Transactions on Graphics (TOG) 37, 4 (2018), 1–16.
- Y. Fei, C. Batty, E. Grinspun, and C. Zheng. 2019. A multi-scale model for coupling strands with shear-dependent liquid. ACM Trans. Graph. 38, 6 (2019), 1–20.
- Yun Fei, Yuhan Huang, and Ming Gao. 2021. Principles towards real-time simulation of material point method on modern GPUs. arXiv preprint arXiv:2111.00699 (2021).
- Y. Fei, H. T. Maia, C. Batty, C. Zheng, and E. Grinspun. 2017. A multi-scale model for simulating liquid-hair interactions. ACM Trans. Graph. 36, 4 (2017), 1–17.
- Ming Gao, Andre Pradhana Tampubolon, Chenfanfu Jiang, and Eftychios Sifakis. 2017. An adaptive generalized interpolation material point method for simulating elastoplastic materials. ACM Transactions on Graphics (TOG) 36, 6 (2017), 1–12.
- Ming Gao, Xinlei Wang, Kui Wu, Andre Pradhana, Eftychios Sifakis, Cem Yuksel, and Chenfanfu Jiang. 2018. GPU optimization of material point methods. ACM Transactions on Graphics (TOG) 37, 6 (2018), 1–12.
- Theodore F Gast, Craig Schroeder, Alexey Stomakhin, Chenfanfu Jiang, and Joseph M Teran. 2015. Optimization integrator for large time steps. *IEEE transactions on visualization and computer graphics* 21, 10 (2015), 1103–1115.
- Johan Gaume, T Gast, J Teran, A Van Herwijnen, and C Jiang. 2018. Dynamic anticrack propagation in snow. Nature communications 9, 1 (2018), 3047.
- Eitan Grinspun, Anil N Hirani, Mathieu Desbrun, and Peter Schröder. 2003. Discrete shells. In ACM SIGGRAPH/Eurographics symposium on Computer animation. 62–67.
- Xuchen Han, Theodore F Gast, Qi Guo, Stephanie Wang, Chenfanfu Jiang, and Joseph Teran. 2019. A hybrid material point method for frictional contact with diverse materials. Proc. ACM Comput. Graph. Interact. Tech. 2, 2 (2019), 1–24.
- J. Hegemann, C. Jiang, C. Schroeder, and J. M. Teran. 2013. A level set method for ductile fracture. In ACM SIGGR. / Eurogr. Symp. Comput. Animat. 193–201.
- Y. Hu, Y. Fang, Z. Ge, Z. Qu, Y. Zhu, A. Pradhana, and C. Jiang. 2018. A moving least squares material point method with displacement discontinuity and two-way rigid body coupling. ACM Trans. Graph. 37, 4 (2018), 1–14.
- Zhiao Huang, Yuanming Hu, Tao Du, Siyuan Zhou, Hao Su, Joshua B Tenenbaum, and Chuang Gan. 2021. Plasticinelab: A soft-body manipulation benchmark with differentiable physics. arXiv preprint arXiv:2104.03311 (2021).
- Geoffrey Irving, Joseph Teran, and Ronald Fedkiw. 2004. Invertible finite elements for robust simulation of large deformation. In ACM SIGGRAPH/Eurographics symposium on Computer animation. 131–140.
- Geoffrey Irving, Joseph Teran, and Ronald Fedkiw. 2006. Tetrahedral and hexahedral invertible finite elements. *Graphical Models* 68, 2 (2006), 66–89.
- Chenfanfu Jiang, Theodore Gast, and Joseph Teran. 2017. Anisotropic elastoplasticity for cloth, knit and hair frictional contact. ACM Trans. Graph. 36, 4 (2017), 1–14.
- Chenfanfu Jiang, Craig Schroeder, Andrew Selle, Joseph Teran, and Alexey Stomakhin. 2015. The affine particle-in-cell method. ACM Trans. Graph. 34, 4 (2015), 1–10.
- C. Jiang, C. Schroeder, J. Teran, A. Stomakhin, and A. Selle. 2016. The material point method for simulating continuum materials. In Acm siggraph 2016 courses. 1–52.
- Theodore Kim, Fernando De Goes, and Hayley Iben. 2019. Anisotropic elasticity for inversion-safety and element rehabilitation. ACM Trans. Graph. 38, 4 (2019), 1–15.
- Gergely Klár, Theodore Gast, Andre Pradhana, Chuyuan Fu, Craig Schroeder, Chenfanfu Jiang, and Joseph Teran. 2016. Drucker-prager elastoplasticity for sand animation. ACM Transactions on Graphics (TOG) 35, 4 (2016), 1–12.
- L. Lan, D. Kaufman, M. Li, C. Jiang, and Y. Yang. 2022. Affine body dynamics: fast, stable and intersection-free simulation of stiff materials. ACM Trans. Graph. 41, 4 (2022), 1–14.
- M. Li, Z. Ferguson, T. Schneider, T. Langlois, D. Zorin, D. Panozzo, C. Jiang, and D. Kaufman. 2020. Incremental potential contact: intersection-and inversion-free,

- large-deformation dynamics. ACM Trans. Graph. 39, 4 (2020), 49.
- Minchen Li, Ming Gao, Timothy Langlois, Chenfanfu Jiang, and Danny M Kaufman. 2019. Decomposed optimization time integrator for large-step elastodynamics. ACM Transactions on Graphics (TOG) 38, 4 (2019), 1–10.
- Minchen Li, Danny M. Kaufman, and Chenfanfu Jiang. 2021. Codimensional Incremental Potential Contact. ACM Trans. Graph. (SIGGRAPH) 40, 4, Article 170 (2021).
- Xuan Li, Yu Fang, Minchen Li, and Chenfanfu Jiang. 2022a. BFEMP: Interpenetration-free MPM–FEM coupling with barrier contact. Computer Methods in Applied Mechanics and Engineering 390 (2022), 114350.
- Xuan Li, Minchen Li, and Chenfanfu Jiang. 2022b. Energetically consistent inelasticity for optimization time integration. ACM Trans. Graph. 41, 4 (2022), 1–16.
- YP Lian, X Zhang, and Y Liu. 2011a. Coupling of finite element method with material point method by local multi-mesh contact method. Computer Methods in Applied Mechanics and Engineering 200, 47-48 (2011), 3482–3494.
- YP Lian, X Zhang, X Zhou, and ZT Ma. 2011b. A FEMP method and its application in modeling dynamic response of reinforced concrete subjected to impact loading. Computer Methods in Applied Mechanics and Engineering 200, 17-20 (2011).
- James F O'brien, Adam W Bargteil, and Jessica K Hodgins. 2002. Graphical modeling and animation of ductile fracture. In Proceedings of the 29th annual conference on Computer graphics and interactive techniques. 291–294.
- James F O'brien and Jessica K Hodgins. 1999. Graphical modeling and animation of brittle fracture. In Proceedings of the 26th annual conference on Computer graphics and interactive techniques. 137–146.
- Matthew Overby, George E Brown, Jie Li, and Rahul Narain. 2017. ADMM ⊋ projective dynamics: Fast simulation of hyperelastic models with dynamic constraints. *IEEE Transactions on Visualization and Computer Graphics* 23, 10 (2017), 2222–2234.
- Yuxing Qiu, Samuel Temple Reeve, Minchen Li, Yin Yang, Stuart Ryan Slattery, and Chenfanfu Jiang. 2023. A Sparse Distributed Gigascale Resolution Material Point Method. ACM Transactions on Graphics 42, 2 (2023), 1–21.
- Daniel Ram, Theodore Gast, Chenfanfu Jiang, Craig Schroeder, Alexey Stomakhin, Joseph Teran, and Pirouz Kavehpour. 2015. A material point method for viscoelastic fluids, foams and sponges. In Proceedings of the 14th ACM SIGGRAPH/Eurographics Symposium on Computer Animation. 157–163.
- Breannan Smith, Fernando De Goes, and Theodore Kim. 2018. Stable neo-hookean flesh simulation. ACM Transactions on Graphics (TOG) 37, 2 (2018), 1–15.
- Al. Stomakhin, C. Schroeder, L. Chai, J. Teran, and A. Selle. 2013. A material point method for snow simulation. ACM Trans. Graph. 32, 4 (2013), 1–10.
- Alexey Stomakhin, Craig Schroeder, Chenfanfu Jiang, Lawrence Chai, Joseph Teran, and Andrew Selle. 2014. Augmented MPM for phase-change and varied materials. ACM Transactions on Graphics (TOG) 33, 4 (2014), 1–11.
- Haozhe Su, Tao Xue, Chengguizi Han, Chenfanfu Jiang, and Mridul Aanjaneya. 2021. A unified second-order accurate in time MPM formulation for simulating viscoelastic liquids with phase change. ACM Transactions on Graphics (TOG) 40, 4 (2021), 1–18.
- Joseph Teran, Eftychios Sifakis, Geoffrey Irving, and Ronald Fedkiw. 2005. Robust quasistatic finite elements and flesh simulation. In ACM SIGGRAPH/Eurographics symposium on Computer animation. 181–190.
- Demetri Terzopoulos, John Platt, Alan Barr, and Kurt Fleischer. 1987. Elastically deformable models. In *Proceedings of the 14th annual conference on Computer graphics and interactive techniques*. 205–214.
- T. Trusty, D. Kaufman, and D. Levin. 2022. Mixed Variational Finite Elements for Implicit, General-Purpose Simulation of Deformables. arXiv:2202.00183 (2022).
- Xinlei Wang, Minchen Li, Yu Fang, Xinxin Zhang, Ming Gao, Min Tang, Danny M Kaufman, and Chenfanfu Jiang. 2020a. Hierarchical optimization time integration for cfl-rate mpm stepping. ACM Transactions on Graphics (TOG) 39, 3 (2020), 1–16.
  X. Wang, Y. Qiu, S. Slattery, Y. Fang, M. Li, S. Zhu, Y. Zhu, M. Tang, D. Manocha, and C.
- X. Wang, Y. Qiu, S. Slattery, Y. Fang, M. Li, S. Zhu, Y. Zhu, M. Tang, D. Manocha, and C. Jiang. 2020b. A massively parallel and scalable multi-GPU material point method. ACM Transactions on Graphics (TOG) 39, 4 (2020), 30–1.
- Chris Wojtan and Greg Turk. 2008. Fast viscoelastic behavior with thin features. In ACM SIGGRAPH 2008 papers. 1–8.
- Joshuah Wolper, Yunuo Chen, Minchen Li, Yu Fang, Ziyin Qu, Jiecong Lu, Meggie Cheng, and Chenfanfu Jiang. 2020. AnisoMPM: Animating anisotropic damage mechanics: Supplemental document. ACM Trans. Graph 39, 4 (2020).
- Joshuah Wolper, Yu Fang, Minchen Li, Jiecong Lu, Ming Gao, and Chenfanfu Jiang. 2019. CD-MPM: continuum damage material point methods for dynamic fracture animation. ACM Transactions on Graphics (TOG) 38, 4 (2019), 1–15.
- Botao Wu, Zhendong Wang, and Huamin Wang. 2022. A GPU-based multilevel additive schwarz preconditioner for cloth and deformable body simulation. ACM Transactions on Graphics (TOG) 41, 4 (2022), 1–14.
- Yonghao Yue, Breannan Smith, Christopher Batty, Changxi Zheng, and Eitan Grinspun. 2015. Continuum foam: A material point method for shear-dependent flows. ACM Transactions on Graphics (TOG) 34, 5 (2015), 1–20.
- Yidong Zhao, Jinhyun Choo, Yupeng Jiang, and Liuchi Li. 2023a. Coupled material point and level set methods for simulating soils interacting with rigid objects with complex geometry. Computers and Geotechnics 163 (2023), 105708.
- Yidong Zhao, Chenfanfu Jiang, and Jinhyun Choo. 2023b. Circumventing volumetric locking in explicit material point methods: A simple, efficient, and general approach. Internat. J. Numer. Methods Engrg. 124, 23 (2023), 5334–5355.



Figure 7: Snow. Soft FEM mushrooms undergoing elastic deformations by the impact of a falling MPM snowball.

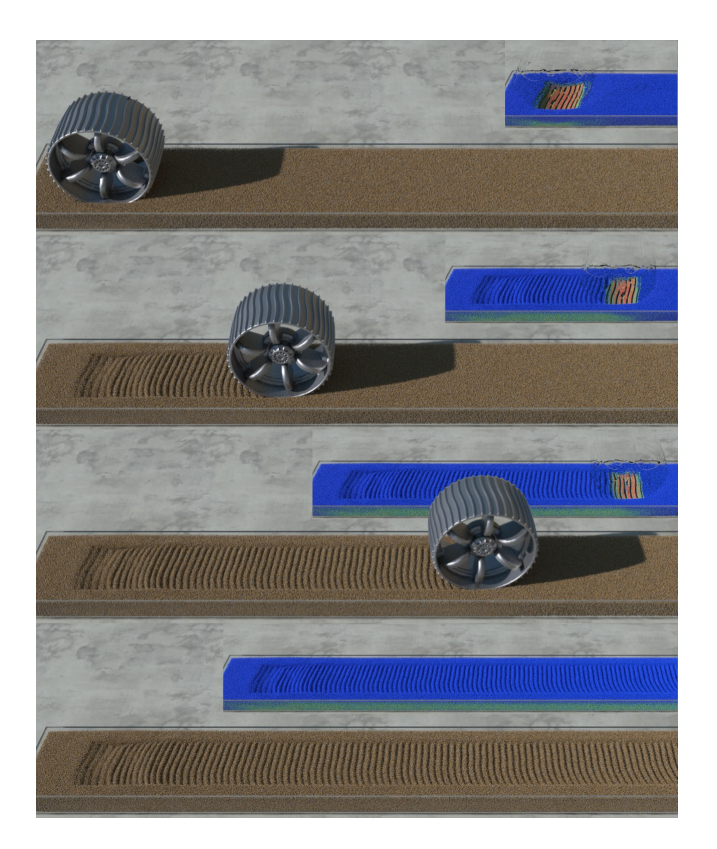


Figure 8: Ruts. The wheel of a Mars rover navigates through the soil and leaves deep ruts in its path. We also visualize the contact force on soil particles, indicated by a color gradient ranging from blue (low) to red (high).

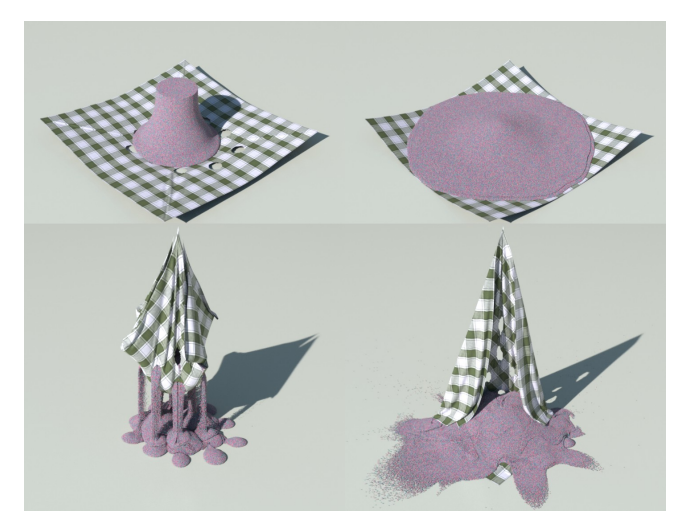


Figure 9: Colored Sand. A pile of MPM sand grains is scooped up by a piece of FEM cloth with holes.

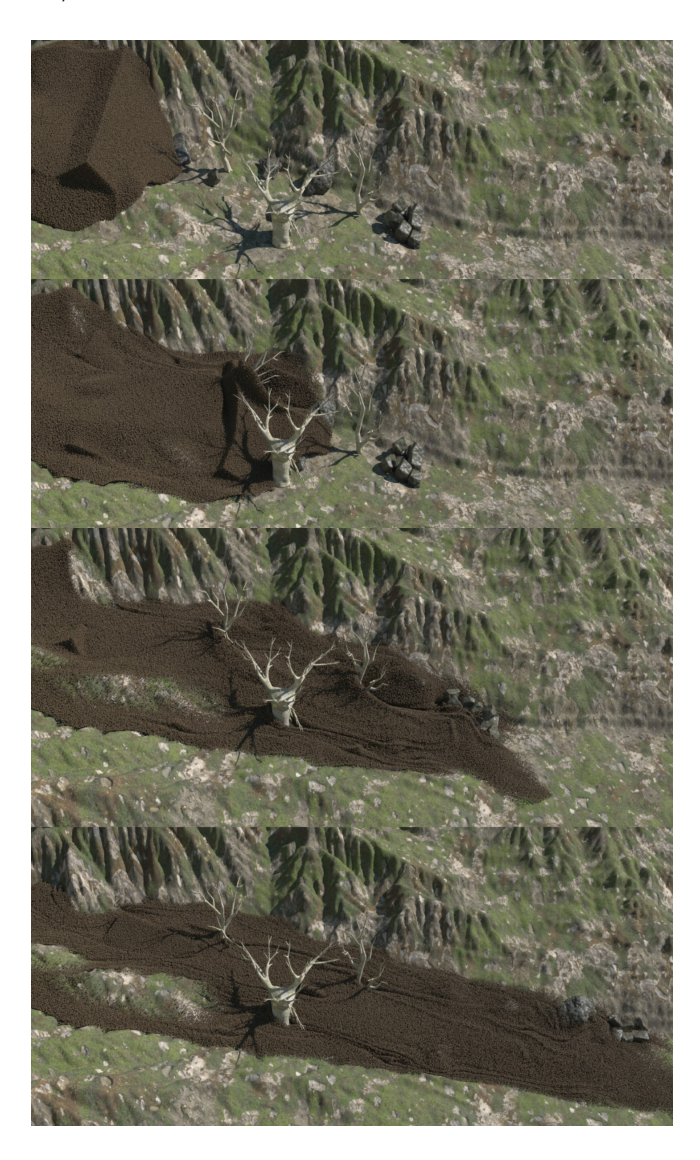


Figure 10: Debris Flow. A large-scale natural disaster caused by debris flow cascading down the valley.